EURODYN 2026
XIII International Conference on Structural Dynamics
M. Beer, C. Papadimitriou, H. Jensen, J. Chen, M. Broggi, J. Behrensdorf (eds.)
Hannover, Germany, 27.09.–01.10 2026

A NOVEL MODEL-ORDER REDUCTION METHOD FOR HYDROELASTIC PERIODIC STRUCTURES WITH STRONG FLUID–STRUCTURE INTERACTION AND SLOSHING WITHIN THE WAVE FINITE ELEMENT METHOD FRAMEWORK

Vinícius Mauro de Souza Santos[1,2], Thiago de Paula Sales[2], and Morvan Ouisse[1]

[1]Aeronautics Institute of Technology, Praça Marechal Eduardo Gomes, 50 – São José dos Campos, 12228-900, SP, Brazil
vinicius.santos@ga.ita.br, thiago.sales@gp.ita.br

[2]Université Marie et Louis Pasteur, SUPMICROTECH, CNRS, Institut FEMTO-ST, Besançon, F-25000, France
morvan.ouisse@femto-st.fr

Keywords: fluid–structure interaction, sloshing, periodic structures, wave-based finite element method, model-order reduction.

Abstract. *Periodic structures have gained considerable attention due to the wide range of functionalities they can offer for wave manipulation. Their study often relies on wave propagation analyses, including the computation of band diagrams, wavemodes, harmonic forced responses, and so forth. Thus, the need for efficient modeling techniques has become crucial to understand their dynamic behavior at an affordable computational cost. In particular, the Wave-based Finite Element Method (WFEM) has emerged as a prominent modeling strategy for the analysis of periodic media, as it enables numerical simulations to be performed without the need to mesh the complete lattice; that is, only a single unit cell of the assembly is analyzed within the WFEM. Although the WFEM fundamentally offers great advantages compared with other simulation techniques, such as the FEM, the analysis of periodic structures by the WFEM can be challenging when unit cells possess many internal and boundary degrees of freedom (DoFs). A large number of internal DoFs in a unit cell causes the dynamic condensation of (internal) DoFs within the WFEM to become very slow or even impossible, while many boundary DoFs increase the complexity of obtaining the so-called wave modes due to the numerous evanescent modes. Model-order reduction has therefore become a key solution for improving the WFEM performance, enabling its application to more complex problems, including those encountered in industrial applications and/or those involving analyses at higher frequencies, which typically require finer meshes and consequently models with a larger number of DoFs. This paper accordingly reports recent advances in the modeling of hydroelastic periodic structures with strong fluid–structure interaction and sloshing, employing reduced-order unit cell models combined with the WFEM. Numerical simulations demonstrate that accurate reduced-order unit cell models can be derived using the proposed model reduction strategy, effectively replacing large-size finite element models, and enabling time-efficient simulations by the WFEM.*

1 INTRODUCTION

Periodic structures are defined as those systems that exhibit some form of periodicity in their architecture, which can be related to material properties, geometric features, or even boundary conditions. Such systems are frequently explored to enable very interesting properties not naturally found in conventional designs. A few ot these properties include: the blocking of wave propagation through the so-called bandgaps [1]; the cloaking of elastic waves, such that wavefronts remain unchanged/unperturbed despite the presence of a defect within the structure [2]; the occurrence of non-reciprocal wave propagation, which breaks reciprocity and therefore causes the system to behave as a diode-like device [3]; and the guidance of acoustic and elastic waves along well-defined wave-paths, enabling active or smart wave control [4].

Currently, investigating these phenomena has been mainly made possible by the continuous advancement in numerical simulations. The Finite Element Method (FEM) is by far one the most widely used modeling strategies for the analysis of periodic media. Notwithstanding, it can be disadvantageous relative to the Wave-based FEM (WFEM) [5, 6]. Within the WFEM, periodic structures are analyzed by considering only a single unit cell characterizing their lattices, i.e., finite media do not need to be discretized into finite elements in their entirety, as one unit cell, together with periodic boundary conditions and the so-called wavemode expansion, is able to deliver similar results. These features make the analysis of periodic structures by the WFEM extremely attractive, thereby motivating research on the topic.

It turns out that some unit cell models may require fine discretization to achieve proper convergence of results within a certain frequency range of analysis, specially when the upper bound of the considered frequency spectrum is high. In practice, a large number of degrees of freedom (DoFs) in a unit cell model makes the WFEM become very computationally expensive and inefficient, leading to increased solution times and memory requirements. Model-order reduction (MOR) thus plays a significant role when addressing large-sized models with the WFEM. Basically, within MOR, a potentially large number of equations of motion (EoMs) encountered in a unit cell physical model is reduced to a set of generalized coordinates, thus yielding a modal model with fewer equations, more manageable within the WFEM [7].

Although MOR is a topic broadly studied and applied across many fields [8–10], deriving reduced-order unit cell models that are subsequently used within the WFEM framework can be challenging in certain cases. Firstly, it should be noted that the unit cell reduced-order models must be derived taking into account that periodic boundary conditions need to be applied afterwards; therefore, so-called compatible modes must be employed during MOR [11]. Secondly, unit cell reduced-order models must accurately reproduce the dynamic characteristics of the full-order models; otherwise, results provided by the WFEM would be incorrect.

Within this work, hydroelastic periodic structures (HPSs) exhibiting strong fluid–structure interactions and linear fluid sloshing are considered. Unit cells are assumed to be made of a compliant geometry, with thin walls and a “soft” material, and the fluid is taken to be mercury, giving rise to strong fluid–structure interactions. Since unit cells are considered to be partially filled with mercury, the fluid free-surface is unconstrained, and therefore complex sloshing phenomena may occur in the fluid domain. Figure 1 illustrates a CAD prototype of the underlying structure, exhibiting six identical unit cells that repeat along the X-direction (dimensions being provided in Section 3). A cut view of the HPS is presented in Fig. 1a, showing that mercury is distributed over the lattice through communicating channels of rectangular geometry; whereas a full view of the structure is presented in Fig. 1b, highlighting the unit cell geometry and the inner mercury in an enlarged, more detailed view.

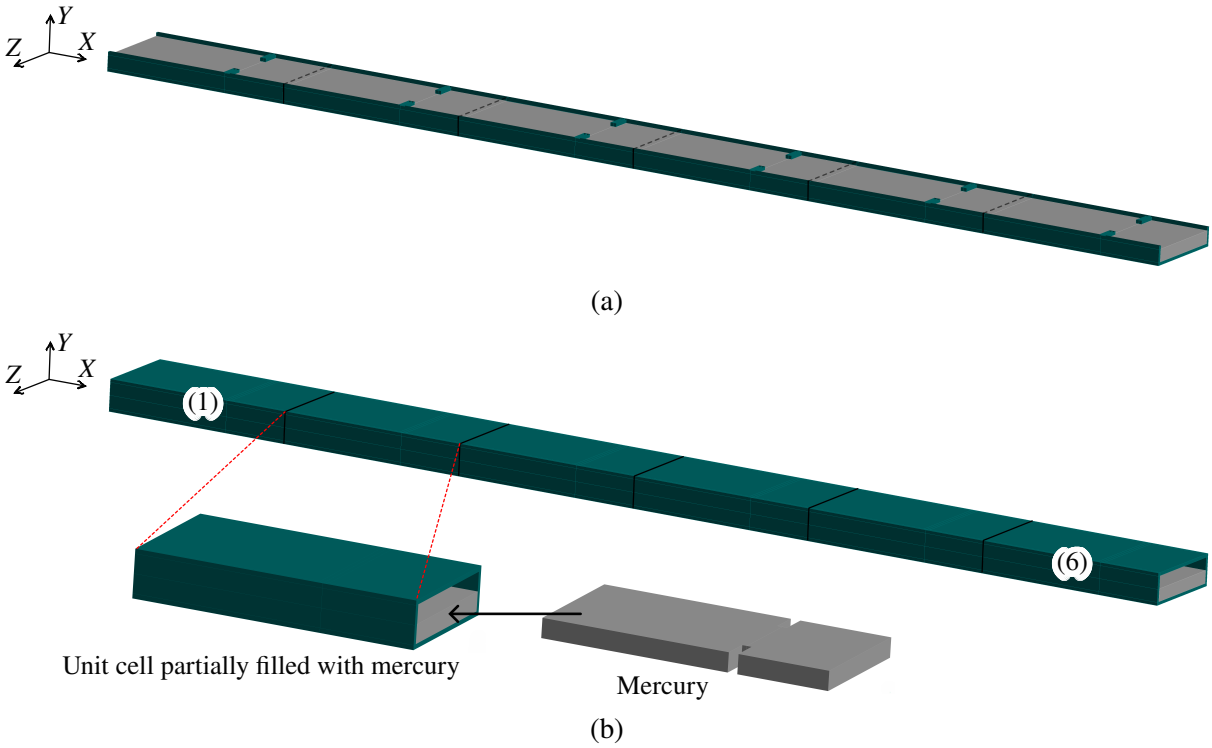


Figure 1: Hydroelastic periodic structure composed of six identical unit cells that repeat along the X-direction: a) cut and b) full views of the lattice.

It has been observed that various MOR strategies currently reported in the literature may fail when applied to hydroelastic unit cell models with strong fluid–structure interactions. This occurs because the majority of such methods have been developed for vibro-acoustic applications, where the coupling strength between air and the elastic medium is usually weak. In addition to this limitation, MOR of vibro-acoustic/hydroelastic problems often suffers from convergence issues [6, 12–14]; that is, very extended (modal) bases are typically required for the reducer-order models to accurately replace their full-order counterparts. So, traditional frequency-based truncation criteria widely used in MOR are not suitable for the selection of eigenvectors in fluid–structure coupled problems. This can be explained by the fact that most MOR approaches applied to vibro-acoustic problems rely on eigenvectors obtained from uncoupled models, which do not properly account for fluid–structure coupling conditions.

Given the issues discussed above, in this study, the MOR of unit cells of HPSs with strong fluid–structure interactions and linear sloshing is conducted using a three-step procedure [15]. First, the unit cell fluid–structure uncoupled internal DoFs are reduced using the Craig–Bampton (CB) method, while preserving DoFs related to fluid–structure interfaces and unit cell boundaries. Afterward, DoFs related to internal fluid–structure interfaces are reduced using local-level characteristic (L-CC) modes, employing three sets of Ritz vectors that account for local and global dynamics. Finally, the unit cell boundary DoFs are also reduced using L-CC modes, ensuring that proper fluid–structure coupling conditions are fulfilled at the unit cell interfaces and constraints related to the Bloch–Floquet theorem can be suitably enforced afterward.

Beyond this introduction, this work is organized as follows: Section 2 addresses the modeling of HPSs by combining size-reduced unit-cell models with the WFEM; results and discussions are presented in Section 3; a summary of the work, along with its main conclusions, is provided in Section 4; and finally, acknowledgments are given in Section 5.

2 MODELING

This section addresses the modeling of HPSs partially filled with fluid, employing reduced-order unit cell models and the WFEM. First, the equations of motion of a single unit cell of a HPS are presented in Subsection 2.1. Then, the three-step MOR procedure is introduced and discussed in Subsections 2.2–2.4. Lastly, the WFEM is reviewed in Subsection 2.5.

2.1 Equations of motion of a unit cell in a hydroelastic periodic structure

The coupled fluid–structure equations of motion for a unit cell such as the one presented in Fig. 1b, considering linear structural behavior, an acoustic model for the fluid, and linear sloshing, read as follows [13]:

$$\begin{bmatrix} \hat{\mathbf{M}}_\mathrm{U} & \mathbf{0} \\ \gamma\rho\,\hat{\mathbf{R}}^\mathrm{T} & \kappa\gamma(\hat{\mathbf{M}}_\mathrm{P}+\hat{\mathbf{M}}_\mathrm{S}) \end{bmatrix} \begin{Bmatrix} \ddot{\hat{\mathbf{q}}}_\mathrm{U} \\ \kappa^{-1}\ddot{\hat{\mathbf{q}}}_\mathrm{P} \end{Bmatrix} + \begin{bmatrix} \hat{\mathbf{K}}_\mathrm{U} & -\kappa\hat{\mathbf{R}} \\ \mathbf{0} & \kappa\gamma\hat{\mathbf{K}}_\mathrm{P} \end{bmatrix} \begin{Bmatrix} \hat{\mathbf{q}}_\mathrm{U} \\ \kappa^{-1}\hat{\mathbf{q}}_\mathrm{P} \end{Bmatrix} = \begin{Bmatrix} \hat{\mathbf{f}}_\mathrm{U} \\ \gamma\hat{\mathbf{f}}_\mathrm{P} \end{Bmatrix}, \tag{1}$$

where $\hat{\mathbf{q}}_\mathrm{U}$ and $\hat{\mathbf{q}}_\mathrm{P}$ are vectors of DoFs related to the structural (U) and acoustic-fluid (P) domains, $\hat{\mathbf{f}}_\mathrm{U}$ and $\hat{\mathbf{f}}_\mathrm{P}$ are the corresponding load vectors, $\hat{\mathbf{M}}_j$ and $\hat{\mathbf{K}}_j$ ($j \in \{\mathrm{U}, \mathrm{P}\}$) are inertia and stiffness matrices, $\hat{\mathbf{M}}_\mathrm{S}$ is the sloshing mass matrix, $\hat{\mathbf{R}}$ is the matrix that couples structural and fluid DoFs, ρ is the fluid density, κ and γ are constants that improve matrix conditioning [16], $(\ \ )^\mathrm{T}$ denotes transposition, and $(\ddot{\ })$ indicates second-order time derivatives.

Equation 1 can be partitioned into DoF sets U_j, P_j, Γ_j ($j \in \{\mathrm{L}, \mathrm{R}, \mathrm{I}\}$), as defined in Fig. 2.

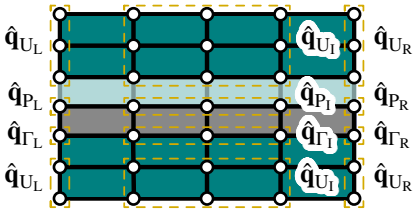


Figure 2: Simplified representation of the finite element mesh of a unit cell of a hydroelastic periodic structure partially filled with fluid (mercury), showing the partitioning of DoFs based on node location (L, R, I) and medium type (U, P). The light green color represents empty space.

Accordingly, the coupled fluid–structure equations of motion can be rewritten as follows:

$$\hat{\mathbf{M}}\ddot{\hat{\mathbf{q}}} + \hat{\mathbf{K}}\hat{\mathbf{q}} = \hat{\mathbf{f}}, \tag{2}$$

where:

$$\hat{\mathbf{q}} = \left\{\hat{\mathbf{q}}_{\mathrm{U_L}}^\mathrm{T} \ \ \hat{\mathbf{q}}_{\mathrm{P_L}}^\mathrm{T} \ \ \hat{\mathbf{q}}_{\Gamma_\mathrm{L}}^\mathrm{T} \ \ \hat{\mathbf{q}}_{\mathrm{U_R}}^\mathrm{T} \ \ \hat{\mathbf{q}}_{\mathrm{P_R}}^\mathrm{T} \ \ \hat{\mathbf{q}}_{\Gamma_\mathrm{R}}^\mathrm{T} \ \ \hat{\mathbf{q}}_{\mathrm{U_I}}^\mathrm{T} \ \ \hat{\mathbf{q}}_{\mathrm{P_I}}^\mathrm{T} \ \ \hat{\mathbf{q}}_{\Gamma_\mathrm{I}}^\mathrm{T}\right\}^\mathrm{T}, \tag{3}$$

$$\hat{\mathbf{f}} = \left\{\hat{\mathbf{f}}_{\mathrm{U_L}}^\mathrm{T} \ \ \hat{\mathbf{f}}_{\mathrm{P_L}}^\mathrm{T} \ \ \hat{\mathbf{f}}_{\Gamma_\mathrm{L}}^\mathrm{T} \ \ \hat{\mathbf{f}}_{\mathrm{U_R}}^\mathrm{T} \ \ \hat{\mathbf{f}}_{\mathrm{P_R}}^\mathrm{T} \ \ \hat{\mathbf{f}}_{\Gamma_\mathrm{R}}^\mathrm{T} \ \ \hat{\mathbf{f}}_{\mathrm{U_I}}^\mathrm{T} \ \ \hat{\mathbf{f}}_{\mathrm{P_I}}^\mathrm{T} \ \ \hat{\mathbf{f}}_{\Gamma_\mathrm{I}}^\mathrm{T}\right\}^\mathrm{T}. \tag{4}$$

2.2 Reduction of uncoupled structural and fluid internal DoFs ($\mathrm{U_I}$ and $\mathrm{P_I}$ DoF sets)

Figure 2 clearly indicates that the $\mathrm{U_I}$ and $\mathrm{P_I}$ DoFs sets are uncoupled due to the fluid–structure interface. Therefore, their reduction can be performed independently within the CB scheme [8], using the following relation:

$$\hat{\mathbf{q}} = \alpha_\mathrm{CB}\tilde{\mathbf{q}}, \tag{5}$$

where:

$$\tilde{\mathbf{q}} = \left\{\hat{\mathbf{q}}_{\mathrm{U_L}}^\mathrm{T} \ \ \hat{\mathbf{q}}_{\mathrm{P_L}}^\mathrm{T} \ \ \hat{\mathbf{q}}_{\Gamma_\mathrm{L}}^\mathrm{T} \ \ \hat{\mathbf{q}}_{\mathrm{U_R}}^\mathrm{T} \ \ \hat{\mathbf{q}}_{\mathrm{P_R}}^\mathrm{T} \ \ \hat{\mathbf{q}}_{\Gamma_\mathrm{R}}^\mathrm{T} \ \ \mathbf{q}_{\mathrm{U_I}}^\mathrm{T} \ \ \mathbf{q}_{\mathrm{P_I}}^\mathrm{T} \ \ \hat{\mathbf{q}}_{\Gamma_\mathrm{I}}^\mathrm{T}\right\}^\mathrm{T}, \tag{6}$$

and the CB projection matrix is given by:

$$\boldsymbol{\alpha}_{\mathrm{CB}} = \begin{bmatrix} \mathbf{I} & \mathbf{0} & \mathbf{0} & \mathbf{0} & \mathbf{0} & \mathbf{0} & \mathbf{0} & \mathbf{0} & \mathbf{0} \\ \mathbf{0} & \mathbf{I} & \mathbf{0} & \mathbf{0} & \mathbf{0} & \mathbf{0} & \mathbf{0} & \mathbf{0} & \mathbf{0} \\ \mathbf{0} & \mathbf{0} & \mathbf{I} & \mathbf{0} & \mathbf{0} & \mathbf{0} & \mathbf{0} & \mathbf{0} & \mathbf{0} \\ \mathbf{0} & \mathbf{0} & \mathbf{0} & \mathbf{I} & \mathbf{0} & \mathbf{0} & \mathbf{0} & \mathbf{0} & \mathbf{0} \\ \mathbf{0} & \mathbf{0} & \mathbf{0} & \mathbf{0} & \mathbf{I} & \mathbf{0} & \mathbf{0} & \mathbf{0} & \mathbf{0} \\ \mathbf{0} & \mathbf{0} & \mathbf{0} & \mathbf{0} & \mathbf{0} & \mathbf{I} & \mathbf{0} & \mathbf{0} & \mathbf{0} \\ \boldsymbol{\Sigma}_{\mathrm{U_I,U_L}} & \boldsymbol{\Sigma}_{\mathrm{U_I,P_L}} & \boldsymbol{\Sigma}_{\mathrm{U_I,\Gamma_L}} & \boldsymbol{\Sigma}_{\mathrm{U_I,U_R}} & \boldsymbol{\Sigma}_{\mathrm{U_I,P_R}} & \boldsymbol{\Sigma}_{\mathrm{U_I,\Gamma_R}} & \boldsymbol{\Xi}_{\mathrm{U_I}} & \mathbf{0} & \boldsymbol{\Sigma}_{\mathrm{U_I,\Gamma_I}} \\ \boldsymbol{\Sigma}_{\mathrm{P_I,U_L}} & \boldsymbol{\Sigma}_{\mathrm{P_I,P_L}} & \boldsymbol{\Sigma}_{\mathrm{P_I,\Gamma_L}} & \boldsymbol{\Sigma}_{\mathrm{P_I,U_R}} & \boldsymbol{\Sigma}_{\mathrm{P_I,P_R}} & \boldsymbol{\Sigma}_{\mathrm{P_I,\Gamma_R}} & \mathbf{0} & \boldsymbol{\Xi}_{\mathrm{P_I}} & \boldsymbol{\Sigma}_{\mathrm{P_I,\Gamma_I}} \\ \mathbf{0} & \mathbf{0} & \mathbf{0} & \mathbf{0} & \mathbf{0} & \mathbf{0} & \mathbf{0} & \mathbf{0} & \mathbf{I} \end{bmatrix}. \tag{7}$$

In the above, $\mathbf{I}$ denotes identity matrices of appropriate sizes, and $\boldsymbol{\Sigma}$ and $\boldsymbol{\Xi}$ refer to matrices of static and fixed-interface modes, respectively [15].

Equation (2) can then be reduced to:

$$\tilde{\mathbf{M}}\ddot{\tilde{\mathbf{q}}} + \tilde{\mathbf{K}}\tilde{\mathbf{q}} = \tilde{\mathbf{f}}, \tag{8}$$

where $\tilde{\mathbf{M}} = \boldsymbol{\alpha}_{\mathrm{CB}}^{\mathrm{T}}\hat{\mathbf{M}}\boldsymbol{\alpha}_{\mathrm{CB}}$, $\tilde{\mathbf{K}} = \boldsymbol{\alpha}_{\mathrm{CB}}^{\mathrm{T}}\hat{\mathbf{K}}\boldsymbol{\alpha}_{\mathrm{CB}}$, and $\tilde{\mathbf{f}} = \boldsymbol{\alpha}_{\mathrm{CB}}^{\mathrm{T}}\hat{\mathbf{f}}$. The number of uncoupled structural and acoustic-fluid DoFs typically reduces significantly due to this procedure. However, numerous DoFs still appear in Eq. (8) because the fluid–structure interfaces and boundary DoFs remain unreduced. Therefore, their reduction is addressed in Subsections 2.3 and 2.4.

2.3 Reduction of coupled structural and fluid internal DoFs ($\boldsymbol{\Gamma}_{\mathbf{I}}$ DoF set)

The reduction of the set of internal DoFs defined by Γ_{I} can be performed using the following relation:

$$\tilde{\mathbf{q}} = \boldsymbol{\alpha}_{\text{L-CC}_{\Gamma_{\mathrm{I}}}}\bar{\mathbf{q}}, \tag{9}$$

where:

$$\bar{\mathbf{q}} = \left\{\hat{\mathbf{q}}_{\mathrm{U_L}}^{\mathrm{T}} \quad \hat{\mathbf{q}}_{\mathrm{P_L}}^{\mathrm{T}} \quad \hat{\mathbf{q}}_{\Gamma_{\mathrm{L}}}^{\mathrm{T}} \quad \hat{\mathbf{q}}_{\mathrm{U_R}}^{\mathrm{T}} \quad \hat{\mathbf{q}}_{\mathrm{P_R}}^{\mathrm{T}} \quad \hat{\mathbf{q}}_{\Gamma_{\mathrm{R}}}^{\mathrm{T}} \quad \mathbf{q}_{\mathrm{U_I}}^{\mathrm{T}} \quad \mathbf{q}_{\mathrm{P_I}}^{\mathrm{T}} \quad \mathbf{q}_{\Gamma_{\mathrm{I}}}^{\mathrm{T}}\right\}^{\mathrm{T}}, \tag{10}$$

and

$$\boldsymbol{\alpha}_{\text{L-CC}_{\Gamma_{\mathrm{I}}}} = \begin{bmatrix} \mathbf{I} & \mathbf{0} \\ \mathbf{0} & \boldsymbol{\Psi}_{\Gamma_{\mathrm{I}}} \end{bmatrix}. \tag{11}$$

Matrix $\boldsymbol{\Psi}_{\Gamma_{\mathrm{I}}}$ above collects three sets of eigenvectors related to local modes (LMs, $\mathbf{L}$), rigid-body modes (RBMs, $\mathbf{R}$), and low-frequency flexible-body modes (FBMs, $\mathbf{F}$) [15, 17]. Since unit cells are partially filled with fluid (cf. Figs. 1 and 2), several sloshing modes (SMs) and non-sloshing modes (N-SMs) arise during the computation of LMs and FBMs. This significantly increases the size of matrix $\boldsymbol{\Psi}_{\Gamma_{\mathrm{I}}}$ and makes the MOR process less-efficient. The numerous SMs, on the other hand, appear to be redundant to some extent in the construction of the projection matrix related to the reduction of internal fluid–structure coupled DoFs, as they arise simultaneously in the LMs and FBMs and may exhibit similar shapes. Therefore, it has been observed that some SMs can be eliminated from $\boldsymbol{\Psi}_{\Gamma_{\mathrm{I}}}$ without compromising the MOR accuracy, such that the following basis can be obtained (with cancellation marks indicating sets of discarded modes):

$$\boldsymbol{\Psi}_{\Gamma_{\mathrm{I}}} = \begin{bmatrix} \overbrace{\cancel{\mathbf{L}_{\Gamma_{\mathrm{I,U}}}^{\mathrm{SMs}}} \quad \mathbf{L}_{\Gamma_{\mathrm{I,U}}}^{\mathrm{N\text{-}SMs}}}^{\text{local modes}} & \overbrace{\mathbf{R}_{\Gamma_{\mathrm{I,U}}} \quad \mathbf{F}_{\Gamma_{\mathrm{I,U}}}^{\mathrm{SMs}} \quad \mathbf{F}_{\Gamma_{\mathrm{I,U}}}^{\mathrm{N\text{-}SMs}}}^{\text{global modes}} & \underbrace{\mathbf{0} \quad \mathbf{0}}_{\text{local modes}} & \underbrace{\mathbf{0} \quad \mathbf{0} \quad \mathbf{0}}_{\text{global modes}} \\ \mathbf{0} \quad \mathbf{0} & \mathbf{0} \quad \mathbf{0} \quad \mathbf{0} & \underbrace{\cancel{\mathbf{L}_{\Gamma_{\mathrm{I,P}}}^{\mathrm{SMs}}} \quad \mathbf{L}_{\Gamma_{\mathrm{I,P}}}^{\mathrm{N\text{-}SMs}}}_{\text{local modes}} & \underbrace{\mathbf{R}_{\Gamma_{\mathrm{I,P}}} \quad \mathbf{F}_{\Gamma_{\mathrm{I,P}}}^{\mathrm{SMs}} \quad \mathbf{F}_{\Gamma_{\mathrm{I,P}}}^{\mathrm{N\text{-}SMs}}}_{\text{global modes}} \end{bmatrix}. \tag{12}$$

Accordingly, Eq. (8) is reduced to:

$$\bar{\mathbf{M}}\ddot{\bar{\mathbf{q}}} + \bar{\mathbf{K}}\bar{\mathbf{q}} = \bar{\mathbf{f}}, \tag{13}$$

where $\bar{\mathbf{M}} = \boldsymbol{\alpha}^{\mathrm{T}}_{\text{L-CC}_{\Gamma_\mathrm{I}}}\tilde{\mathbf{M}}\boldsymbol{\alpha}_{\text{L-CC}_{\Gamma_\mathrm{I}}}$, $\bar{\mathbf{K}} = \boldsymbol{\alpha}^{\mathrm{T}}_{\text{L-CC}_{\Gamma_\mathrm{I}}}\tilde{\mathbf{K}}\boldsymbol{\alpha}_{\text{L-CC}_{\Gamma_\mathrm{I}}}$, and $\bar{\mathbf{f}} = \boldsymbol{\alpha}^{\mathrm{T}}_{\text{L-CC}_{\Gamma_\mathrm{I}}}\tilde{\mathbf{f}}$. At this point, all interior DoFs of the unit cell model have been replaced by modal quantities. The reduction of boundary DoFs, involving uncoupled structural and fluid DoFs, as well as fluid–structure coupled DoFs (cf. Fig. 2), is discussed in the following subsection.

2.4 Reduction of boundary DoFs ($\mathbf{U_L}$, $\mathbf{P_L}$, $\boldsymbol{\Gamma}_\mathbf{L}$, $\mathbf{U_R}$, $\mathbf{P_R}$, and $\boldsymbol{\Gamma}_\mathbf{R}$ DoF sets)

Lastly, the unit cell boundary DoFs are reduced using the L-CC method [7], for which the following relation between partially and fully reduced DoF sets applies:

$$\bar{\mathbf{q}} = \boldsymbol{\alpha}_{\text{L-CC}_\mathrm{B}}\mathbf{q}, \tag{14}$$

where:

$$\mathbf{q} = \left\{\mathbf{q}^{\mathrm{T}}_{\mathrm{U_L}} \;\; \mathbf{q}^{\mathrm{T}}_{\mathrm{P_L}} \;\; \mathbf{q}^{\mathrm{T}}_{\Gamma_\mathrm{L}} \;\; \mathbf{q}^{\mathrm{T}}_{\mathrm{U_R}} \;\; \mathbf{q}^{\mathrm{T}}_{\mathrm{P_R}} \;\; \mathbf{q}^{\mathrm{T}}_{\Gamma_\mathrm{R}} \;\; \mathbf{q}^{\mathrm{T}}_{\mathrm{U_I}} \;\; \mathbf{q}^{\mathrm{T}}_{\mathrm{P_I}} \;\; \mathbf{q}^{\mathrm{T}}_{\Gamma_\mathrm{I}}\right\}^{\mathrm{T}}, \tag{15}$$

and

$$\boldsymbol{\alpha}_{\text{L-CC}_\mathrm{B}} = \begin{bmatrix}
\boldsymbol{\Psi}_{\mathrm{U_{LR}}} & \mathbf{0} & \mathbf{0} & \mathbf{0} & \mathbf{0} & \mathbf{0} & \mathbf{0} & \mathbf{0} & \mathbf{0} \\
\mathbf{0} & \boldsymbol{\Psi}_{\mathrm{P_{LR}}} & \mathbf{0} & \mathbf{0} & \mathbf{0} & \mathbf{0} & \mathbf{0} & \mathbf{0} & \mathbf{0} \\
\mathbf{0} & \mathbf{0} & \boldsymbol{\Psi}_{\Gamma_{\mathrm{LR}}} & \mathbf{0} & \mathbf{0} & \mathbf{0} & \mathbf{0} & \mathbf{0} & \mathbf{0} \\
\mathbf{0} & \mathbf{0} & \mathbf{0} & \boldsymbol{\Psi}_{\mathrm{U_{LR}}} & \mathbf{0} & \mathbf{0} & \mathbf{0} & \mathbf{0} & \mathbf{0} \\
\mathbf{0} & \mathbf{0} & \mathbf{0} & \mathbf{0} & \boldsymbol{\Psi}_{\mathrm{P_{LR}}} & \mathbf{0} & \mathbf{0} & \mathbf{0} & \mathbf{0} \\
\mathbf{0} & \mathbf{0} & \mathbf{0} & \mathbf{0} & \mathbf{0} & \boldsymbol{\Psi}_{\Gamma_{\mathrm{LR}}} & \mathbf{0} & \mathbf{0} & \mathbf{0} \\
\mathbf{0} & \mathbf{0} & \mathbf{0} & \mathbf{0} & \mathbf{0} & \mathbf{0} & \mathbf{I} & \mathbf{0} & \mathbf{0} \\
\mathbf{0} & \mathbf{0} & \mathbf{0} & \mathbf{0} & \mathbf{0} & \mathbf{0} & \mathbf{0} & \mathbf{I} & \mathbf{0} \\
\mathbf{0} & \mathbf{0} & \mathbf{0} & \mathbf{0} & \mathbf{0} & \mathbf{0} & \mathbf{0} & \mathbf{0} & \mathbf{I}
\end{bmatrix}. \tag{16}$$

The matrices $\boldsymbol{\Psi}_{\mathrm{U_{LR}}}$, $\boldsymbol{\Psi}_{\mathrm{P_{LR}}}$, and $\boldsymbol{\Psi}_{\Gamma_{\mathrm{LR}}}$ above denote augmented eigenvector bases used in MOR [15]. Particularly, $\boldsymbol{\Psi}_{\mathrm{U_{LR}}}$ and $\boldsymbol{\Psi}_{\mathrm{P_{LR}}}$ collect eigenvector partitions related to global modes (RBMs and FBMs), previously used in the assembly of $\boldsymbol{\Psi}_{\Gamma_\mathrm{I}}$, accounting for left (L) and right (R) interface modes, and take the following form after distinguishing eigenvectors into SMs and N-SMs:

$$\boldsymbol{\Psi}_{\mathrm{U_{LR}}} = \begin{bmatrix} \cancel{\tilde{\boldsymbol{\phi}}^{\text{SMs}}_{\mathrm{U_{L_1}}}} & \cdots & \cancel{\tilde{\boldsymbol{\phi}}^{\text{SMs}}_{\mathrm{U_{L_\star}}}} & \tilde{\boldsymbol{\phi}}^{\text{N-SMs}}_{\mathrm{U_{L_1}}} & \cdots & \tilde{\boldsymbol{\phi}}^{\text{N-SMs}}_{\mathrm{U_{L_\star}}} & \cancel{\tilde{\boldsymbol{\phi}}^{\text{SMs}}_{\mathrm{U_{R_1}}}} & \cdots & \cancel{\tilde{\boldsymbol{\phi}}^{\text{SMs}}_{\mathrm{U_{R_\star}}}} & \tilde{\boldsymbol{\phi}}^{\text{N-SMs}}_{\mathrm{U_{R_1}}} & \cdots & \tilde{\boldsymbol{\phi}}^{\text{N-SMs}}_{\mathrm{U_{R_\star}}} \end{bmatrix}, \tag{17}$$

$$\boldsymbol{\Psi}_{\mathrm{P_{LR}}} = \begin{bmatrix} \tilde{\boldsymbol{\phi}}^{\text{SMs}}_{\mathrm{P_{L_1}}} & \cdots & \tilde{\boldsymbol{\phi}}^{\text{SMs}}_{\mathrm{P_{L_\star}}} & \tilde{\boldsymbol{\phi}}^{\text{N-SMs}}_{\mathrm{P_{L_1}}} & \cdots & \tilde{\boldsymbol{\phi}}^{\text{N-SMs}}_{\mathrm{P_{L_\star}}} & \tilde{\boldsymbol{\phi}}^{\text{SMs}}_{\mathrm{P_{R_1}}} & \cdots & \tilde{\boldsymbol{\phi}}^{\text{SMs}}_{\mathrm{P_{R_\star}}} & \tilde{\boldsymbol{\phi}}^{\text{N-SMs}}_{\mathrm{P_{R_1}}} & \cdots & \tilde{\boldsymbol{\phi}}^{\text{N-SMs}}_{\mathrm{P_{R_\star}}} \end{bmatrix}, \tag{18}$$

where $\star$ denotes the number of retained vectors in each eigenvector group and cancellation marks indicate discarded sets of eigenvectors.

Regarding $\boldsymbol{\Psi}_{\Gamma_{\mathrm{LR}}}$, it is defined similarly to Eq. (12), this time taking into account left and right interface modes:

$$\boldsymbol{\Psi}_{\Gamma_{\mathrm{LR}}} = \begin{bmatrix} \boldsymbol{\Psi}_{\Gamma_{\text{LR-U}}} & \mathbf{0} \\ \mathbf{0} & \boldsymbol{\Psi}_{\Gamma_{\text{LR-P}}} \end{bmatrix}, \tag{19}$$

where:

$$\boldsymbol{\Psi}_{\Gamma_{\text{LR-U}}} = \Big[\overbrace{\cancel{\mathbf{L}^{\text{SMs}}_{\Gamma_{\mathrm{L,U}}}} \;\; \mathbf{L}^{\text{N-SMs}}_{\Gamma_{\mathrm{L,U}}} \;\; \cancel{\mathbf{L}^{\text{SMs}}_{\Gamma_{\mathrm{R,U}}}} \;\; \mathbf{L}^{\text{N-SMs}}_{\Gamma_{\mathrm{R,U}}}}^{\text{local modes}} \;\; \overbrace{\mathbf{R}_{\Gamma_{\mathrm{L,U}}} \;\; \mathbf{R}_{\Gamma_{\mathrm{R,U}}} \;\; \cancel{\mathbf{F}^{\text{SMs}}_{\Gamma_{\mathrm{L,U}}}} \;\; \mathbf{F}^{\text{N-SMs}}_{\Gamma_{\mathrm{L,U}}} \;\; \cancel{\mathbf{F}^{\text{SMs}}_{\Gamma_{\mathrm{R,U}}}} \;\; \mathbf{F}^{\text{N-SMs}}_{\Gamma_{\mathrm{R,U}}}}^{\text{global modes}}\Big], \tag{20}$$

$$\boldsymbol{\Psi}_{\Gamma_{\text{LR-P}}} = \Big[\overbrace{\cancel{\mathbf{L}^{\text{SMs}}_{\Gamma_{\text{L,P}}}} \quad \mathbf{L}^{\text{N-SMs}}_{\Gamma_{\text{L,P}}} \quad \cancel{\mathbf{L}^{\text{SMs}}_{\Gamma_{\text{R,P}}}} \quad \mathbf{L}^{\text{N-SMs}}_{\Gamma_{\text{R,P}}}}^{\text{local modes}} \overbrace{\mathbf{R}_{\Gamma_{\text{L,P}}} \quad \mathbf{R}_{\Gamma_{\text{R,P}}} \quad \mathbf{F}^{\text{SMs}}_{\Gamma_{\text{L,P}}} \quad \mathbf{F}^{\text{N-SMs}}_{\Gamma_{\text{L,P}}} \quad \mathbf{F}^{\text{SMs}}_{\Gamma_{\text{R,P}}} \quad \mathbf{F}^{\text{N-SMs}}_{\Gamma_{\text{R,P}}}}^{\text{global modes}}\Big]. \tag{21}$$

In the above, the global modes are obtained in the same manner as those used to assemble $\boldsymbol{\Psi}_{\Gamma_{\text{I}}}$, $\boldsymbol{\Psi}_{\text{U}_{\text{LR}}}$, and $\boldsymbol{\Psi}_{\text{P}_{\text{LR}}}$, whereas the determination of local modes involve solving additional eigenvalue problems defined by the matrix pencils $(\bar{\mathbf{K}}_{\Gamma_{\text{L}},\Gamma_{\text{L}}}, \bar{\mathbf{M}}_{\Gamma_{\text{L}},\Gamma_{\text{L}}})$ and $(\bar{\mathbf{K}}_{\Gamma_{\text{R}},\Gamma_{\text{R}}}, \bar{\mathbf{M}}_{\Gamma_{\text{R}},\Gamma_{\text{R}}})$.

After determining suitable bases for the reduction of boundary DoFs, Eq. (13) is projected onto the reduced space, yielding:

$$\mathbf{M}\ddot{\mathbf{q}} + \mathbf{K}\mathbf{q} = \mathbf{f}, \tag{22}$$

where $\mathbf{M} = \boldsymbol{\alpha}^{\text{T}}_{\text{L-CC}_{\text{B}}}\bar{\mathbf{M}}\boldsymbol{\alpha}_{\text{L-CC}_{\text{B}}}$, $\mathbf{K} = \boldsymbol{\alpha}^{\text{T}}_{\text{L-CC}_{\text{B}}}\bar{\mathbf{K}}\boldsymbol{\alpha}_{\text{L-CC}_{\text{B}}}$, and $\mathbf{f} = \boldsymbol{\alpha}^{\text{T}}_{\text{L-CC}_{\text{B}}}\bar{\mathbf{f}}$. Since $\mathbf{q}$ in Eq. (22) is defined in Eq. (15), it can be observed that no physical DoFs remain, i.e., only modal/generalized DoFs are involved. Accordingly, the reduced-order unit cell model given in Eq. (22) can be subsequently incorporated into the WFEM framework.

2.5 The Wave-based Finite Element Method applied to hydroelastic periodic structures

Within the WFEM, Eq. (22) is first cast into a symmetric formulation based on the acoustic velocity potential φ [18], such that the following can be obtained in the frequency domain:

$$\left(-\omega^2\begin{bmatrix}\mathbf{M}_{\text{U}} & \mathbf{0}\\ \mathbf{0} & -\rho\mathbf{M}_{\text{P}}\end{bmatrix} + \text{i}\omega\begin{bmatrix}\mathbf{0} & \rho\mathbf{R}\\ \rho\,\mathbf{R}^{\text{T}} & \mathbf{0}\end{bmatrix} + \begin{bmatrix}\mathbf{K}_{\text{U}} & \mathbf{0}\\ \mathbf{0} & -\rho\mathbf{K}_{\text{P}}\end{bmatrix}\right)\begin{Bmatrix}\mathbf{Q}_{\text{U}}\\ \mathbf{Q}_{\varphi}\end{Bmatrix} = \begin{Bmatrix}\mathbf{F}_{\text{U}}\\ \mathbf{F}_{\varphi}\end{Bmatrix}, \tag{23}$$

where $\mathbf{Q}_{\text{U}}$, $\mathbf{Q}_{\varphi}$, $\mathbf{F}_{\text{U}}$ and $\mathbf{F}_{\varphi}$ respectively denote the frequency domain amplitudes associated with $\mathbf{q}_{\text{U}}$, $\mathbf{q}_{\varphi}$, $\mathbf{f}_{\text{U}}$ and $\mathbf{f}_{\varphi}$, ω is the circular frequency, and $\text{i} = \sqrt{-1}$.

It can be demonstrated that Eq. (23) leads to [5]:

$$\mathbf{u}^{(n+1)}_{\text{L}} = \mathbf{S}\mathbf{u}^{(n)}_{\text{L}} + \mathbf{b}^{(n)}, \tag{24}$$

where $\mathbf{u}_{\text{L}}$ is the unit cell state vector, $\mathbf{S}$ is the unit cell symplectic transfer matrix, and $\mathbf{b}$ is a vector related to externally applied loads. The superscripts (n), $(n+1)$ indicate unit cell numbers.

Upon consideration of null external loads and the Bloch–Floquet theorem, it follows that [6]:

$$\left(\mathbf{S} - \mu_j\mathbf{I}\right)\boldsymbol{\phi}_j = \mathbf{0}, \qquad \text{where} \qquad \mu_j = \exp(-\text{i}k_j\Delta), \qquad \text{for } j \in \{1, \ldots 2n_{\text{B}}\}. \tag{25}$$

In the above, μ_j and $\boldsymbol{\phi}_j$ denote the so-called wave mode pairs, i.e., the propagation constants and wavemodes/wave shapes, k_j corresponds to the j-th Bloch wavenumber, Δ refers to the unit cell length along the X-direction (cf. Fig. 1), and n_{B} denotes the amount of (modal/generalized) DoFs at the left or right interface of the unit cell.

Due to numerical issues when computing μ_j and $\boldsymbol{\phi}_j$ from Eq. (25), alternative eigenvalue problems are available in the literature. In this study, the Zhong-Williams' $\mathbf{S} + \mathbf{S}^{-1}$ eigenvalue problem is adopted to obtain the wave mode pairs, as it applies to both symmetric and asymmetric unit cell designs and it is less prone to numerical instabilities [19].

After their determination, μ_j and $\boldsymbol{\phi}_j$ can be organized into matrices:

$$\boldsymbol{\mu} = \text{diag}(\mu_1, \ \ldots, \ \mu_{n_{\text{B}}}), \qquad \boldsymbol{\mu}^* = \text{diag}(\mu^*_1, \ \ldots, \ \mu^*_{n_{\text{B}}}), \tag{26}$$

$$\boldsymbol{\Phi} = \begin{bmatrix}\boldsymbol{\phi}_1 & \ldots & \boldsymbol{\phi}_{n_{\text{B}}}\end{bmatrix} = \begin{bmatrix}\boldsymbol{\Phi}_{\text{Q}}\\ \boldsymbol{\Phi}_{\text{F}}\end{bmatrix}, \qquad \boldsymbol{\Phi}^* = \begin{bmatrix}\boldsymbol{\phi}^*_1 & \ldots & \boldsymbol{\phi}^*_{n_{\text{B}}}\end{bmatrix} = \begin{bmatrix}\boldsymbol{\Phi}^*_{\text{Q}}\\ \boldsymbol{\Phi}^*_{\text{F}}\end{bmatrix}, \tag{27}$$

which distinguish the propagation constants and wave shapes according to the direction of wave propagation, i.e., from left to right ($\boldsymbol{\mu}$, $\boldsymbol{\Phi}$) and from right to left ($\boldsymbol{\mu}^*$, $\boldsymbol{\Phi}^*$), while also classifying the wave shapes into partitions related to DoFs (Q) and loads (F).

Afterward, starting from wavemode expansion of $\mathbf{u}_{\mathrm{L}}^{(n)}$ and $\mathbf{b}^{(n)}$, together with orthogonalization conditions, the following expressions can be derived [5]:

$$\mathbf{Q}_{\mathrm{L}}^{(n)} = \boldsymbol{\Phi}_{\mathrm{Q}}\boldsymbol{\mu}^{n-1}\mathbf{Q} + \boldsymbol{\Phi}_{\mathrm{Q}}^{*}\boldsymbol{\mu}^{N+1-n}\mathbf{Q}^{*} + \boldsymbol{\Phi}_{\mathrm{Q}}\sum_{k=1}^{n-1}\boldsymbol{\mu}^{n-k-1}\mathbf{Q}_{\mathrm{B}}^{(k)} - \boldsymbol{\Phi}_{\mathrm{Q}}^{*}\sum_{k=n}^{N}\boldsymbol{\mu}^{k+1-n}\mathbf{Q}_{\mathrm{B}}^{*(k)}, \quad (28)$$

$$-\mathbf{F}_{\mathrm{L}}^{(n)} = \boldsymbol{\Phi}_{\mathrm{F}}\boldsymbol{\mu}^{n-1}\mathbf{Q} + \boldsymbol{\Phi}_{\mathrm{F}}^{*}\boldsymbol{\mu}^{N+1-n}\mathbf{Q}^{*} + \boldsymbol{\Phi}_{\mathrm{F}}\sum_{k=1}^{n-1}\boldsymbol{\mu}^{n-k-1}\mathbf{Q}_{\mathrm{B}}^{(k)} - \boldsymbol{\Phi}_{\mathrm{F}}^{*}\sum_{k=n}^{N}\boldsymbol{\mu}^{k+1-n}\mathbf{Q}_{\mathrm{B}}^{*(k)}, \quad (29)$$

in which N denotes the number of unit cells used to assemble the HPS ($N = 6$ in Fig. 1), $\mathbf{Q}_{\mathrm{B}}$ and $\mathbf{Q}_{\mathrm{B}}^{*(k)}$ are wavemode amplitudes related to external loads, and $\mathbf{Q}$ and $\mathbf{Q}^*$ are wavemode amplitudes of waves propagating from the left interface of the 1st unit cell to the right and from the right interface of the N-th unit cell to the left, respectively.

Equations (28) and (29) can then be used together with prescribed boundary conditions, allowing a frequency-dependent linear system of equations in $\mathbf{Q}$ and $\mathbf{Q}^*$ to be written. In this study, free–free boundary conditions are considered, for which $\mathbf{F}_{\mathrm{L}}^{(1)} = \mathbf{0}$ and $\mathbf{F}_{\mathrm{L}}^{(N+1)} = \mathbf{0}$ hold [20]. An external harmonic force is applied exploring $\mathbf{b}^{(n)}$. Structural ($\mathbf{Q}_{\mathrm{U}}$) and acoustic velocity potential ($\mathbf{Q}_{\varphi}$) amplitudes and/or loads ($\mathbf{F}_{\mathrm{U}}$, $\mathbf{F}_{\varphi}$) can subsequently be retrieved from Eqs. (28) and (29) themselves. Pressure-like responses are recovered from $\mathbf{Q}_{\varphi}$ as $\mathbf{Q}_{\mathrm{P}} = -\mathrm{i}\omega\rho\mathbf{Q}_{\varphi}$. Lastly, responses in physical coordinates can be determined from the (frequency-dependent) modal amplitudes by employing the projection matrices presented previously in Subsections 2.2–2.4.

3 RESULTS AND DISCUSSIONS

This section illustrates the application of the theory introduced in the previous section for the analysis of the HPS presented earlier in Fig. 1. First, the case study is described in detail, and the EoMs for a single unit cell of the HPS are established as in Subsection 2.1. Then, a reduced-order model is derived for the underlying unit cell, in accordance with the theory outlined in Subsections 2.2–2.4. Frequency response functions (FRFs) are computed using the unit cell reduced-order model and the WFEM, as discussed in Subsection 2.5, and the FEM. To quantify the accuracy of the reduced-order unit cell model, relative errors (REs) are calculated between resonance frequencies identified from FRFs computed using the WFEM and FRFs computed with the FEM. Cross-signature scale factors (CSFs) between FRFs obtained using the WFEM and the FEM are also determined for the same purpose. Lastly, a summary of the simulation time is provided to evaluate the performance of the WFEM relative to the traditional FEM.

The unit cell design considered in this study is inspired by the geometry introduced in [21]. Nevertheless, it has been modified to enable stronger fluid–structure interactions and a more general test-case that features, for instance, structural and fluid media simultaneously in the unit cell interior and boundaries. Compared to the design considered in [21], all unit cell walls here have a reduced thickness of 1 mm. In addition, rectangular communicating channels with dimensions of 16 mm × 4 mm and a depth of 1 mm each have been included at the left and right interfaces of the unit cell. In order to make the unit cell design asymmetric, and thus investigate possible limitations of the MOR strategy in this regard, it has been shifted by $\Delta/3$ along the direction of wave propagation (X-direction), resulting in the "shifted" unit cell displayed previously in Fig. 1. By doing so, the communicating channels previously located at the left and right interfaces of the unit cell have been moved to its interior, resulting in a single channel with a depth of 2 mm. Moreover, the fluid has been taken as mercury, characterized by a density of 13529 kg m^{-3} and a

sound speed of 1450 m s^{-1}, while the structural domain is made of polylactic acid (PLA), characterized by a density of 1200 kg m^{-3}, an elastic modulus of 2 GPa, a Poisson's ratio of 0.38, and a hysteretic damping factor of 1% ($\mathbf{K}_{\mathrm{U}} \leftarrow (1 + 0.01\,\mathrm{i})\mathbf{K}_{\mathrm{U}}$). Figure 3 summarizes the resulting unit cell geometry and dimensions (mm).

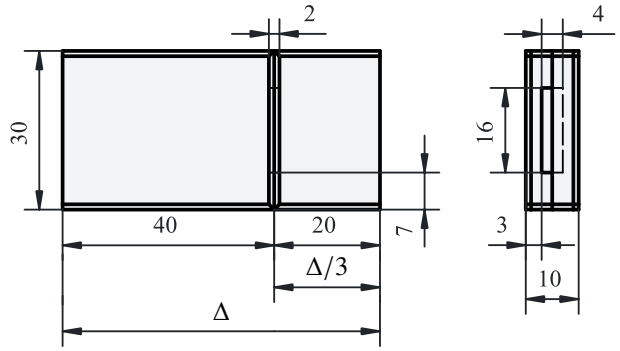


Figure 3: Geometry and dimensions (mm) of the unit cell of the hydroelastic periodic structure previously introduced in Fig. 1.

Accordingly, a finite HPS composed of six identical unit cells ($N = 6$) is considered to perform simulations with the WFEM and FEM, cf. Fig. 1. The unit cell global element size is taken as 2 mm, which largely ensures model convergence up to the maximum frequency of interest, set to 1000 Hz. Figure 4 illustrates the location where the harmonic input force is applied to the HPS, in the positive Y-direction, as well as the locations where the responses are subsequently evaluated. Particularly, the responses are examined for both structural and fluid DoFs, corresponding to nodes located i) at the rightmost end of the HPS (output acceleration), ii) at the rightmost end of the HPS, but at the fluid free-surface (output pressure #1), and iii) within the fluid domain, exactly at the center of the fluid-filled region of the communicating channel (output pressure #2). Note that the structure is rotated by 180° about the XZ plane in Fig. 4 to facilitate the visualization of the output locations, which would otherwise be hidden if the view of Fig. 1 was adopted.

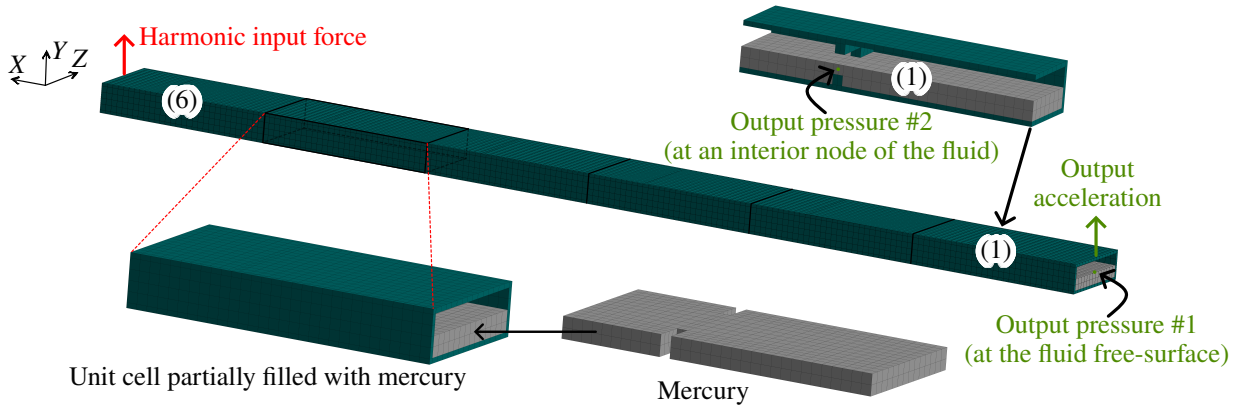


Figure 4: Hydroelastic periodic structure partially filled with mercury ($N = 6$), along with the input and output locations used to compute forced responses. A detailed view of the unit cell making the lattice is provided at the figure bottom, highlighting the mercury shape.

First of all, the EoMs of one unit cell of the HPS presented in Fig. 4 have been obtained using the ANSYS® finite element software, resulting in Eq. (1) after application of the pre-

conditioning procedure [16]. These equations were then reduced according to the methodology introduced throughout Subsections 2.2–2.4, employing frequency-based truncation criterion to retain eigenvectors deemed most important within the projection matrices. Particularly, the eigenvectors used for MOR have been selected such that their eigenvalues lie below or are equal to $n \times 1000\,\text{Hz}$, where n is denoted as n_{CB} for the reduction of uncoupled structural and acoustic-fluid internal DoFs (Subsection 2.2), $n_{\text{L-CC}_\text{I}}$ for the reduction of coupled structural and acoustic-fluid internal DoFs (Subsection 2.3), and $n_{\text{L-CC}_\text{B}}$ for the reduction of boundary DoFs (Subsection 2.4). In this study, these multipliers have been set to $n_{\text{CB}} = 5$, $n_{\text{L-CC}_\text{B}} = 5$, and $n_{\text{L-CC}_\text{I}} = 2$, in accordance with [15].

The classification of eigenvectors as SMs or N-SMs is performed according to the pressure distribution in the acoustic-fluid. If a mode exhibits nodal relative pressures close to zero at the fluid free-surface, then it is classified as a N-SM. Conversely, SMs correspond to those eigenvectors for which the magnitudes of the pressure distribution at the fluid free-surface are not nil. In practice, the ratio between the L^1 norms of all nodal pressures not on the fluid free-surface and of the nodal pressures of all acoustic-fluid nodes is computed. If this ratio is lower than or equal to $\tau_{\text{SMs}} = 99\%$ for a given eigenvector, then it is classified as a SM. Finally, in order to ensure that almost collinear eigenvectors are removed from bases associated with the reduction of boundary DoFs ($\boldsymbol{\Psi}_{\text{U}_\text{LR}}$, $\boldsymbol{\Psi}_{\text{P}_\text{LR}}$ and $\boldsymbol{\Psi}_{\Gamma_\text{LR}}$), a modal assurance criterion-based strategy is adopted to filter-out "redundant" modes [7, 15], for which the MAC threshold is set to $\tau_{\text{MAC}} = 0.90$. Table 1 summarizes the number of physical and modal DoFs for the unit cell finite element model shown in Fig. 4.

	Set of DoFs									
	U_L	P_L	Γ_L	U_R	P_R	Γ_R	U_I	P_I	Γ_I	Total
Physical (full-order model)	489	80	148	489	80	148	21519	3773	7372	34098
Modal (reduced-order model)	38	80	71	38	80	71	4	1189	3283	4854

Table 1: Number of physical and modal DoFs for the unit cell finite element model shown in Fig. 4 ($n_{\text{CB}} = 5$, $n_{\text{L-CC}_\text{I}} = 5$, $n_{\text{L-CC}_\text{B}} = 2$, $\tau_{\text{SMs}} = 0.99$, and $\tau_{\text{MAC}} = 0.90$).

As one may observe from Table 1, during the reduction of uncoupled structural and acoustic-fluid internal DoFs, 21519 and 3773 equations respectively related to the U_I and P_I DoF sets are reduced to 4 and 1189, respectively. The large number of modal DoFs describing the fluid domain arises because all SMs are included in the matrix of acoustic-fluid fixed-interface modes $\boldsymbol{\Xi}_{\text{P}_\text{I}}$ (cf. Subsection 2.2), totaling 1189 for the considered unit cell geometry and mesh. The coupled structural and acoustic-fluid internal DoFs (Γ_I DoF set) are reduced from 7372 physical DoFs to 3283 generalized coordinates. In the present case, the large number of modal DoFs related to the Γ_I DoF set arises not only as a consequence of the SMs included in matrix $\boldsymbol{\Psi}_{\Gamma_\text{I}}$, but also from the need to consider both local and global modes for the proper description of fluid–structure coupled dynamics [17]. Lastly, Table 1 shows that 717 boundary DoFs (U_L, P_L, Γ_L, U_R, P_R, and Γ_R DoF sets) are reduced to 189 modal/generalized coordinates. In total, 34098 physical DoFs are replaced by 4854 modal DoFs using the MOR theory proposed in this work, corresponding to a reduction of more than 85% in the number of equations of the unit cell.

Employing the unit cell reduced-order model, forced responses can be computed within the WFEM framework, as discussed in Subsection 2.5. Accordingly, Fig. 5 shows FRFs computed by the FEM and WFEM, considering the input and output locations presented in Fig. 4.

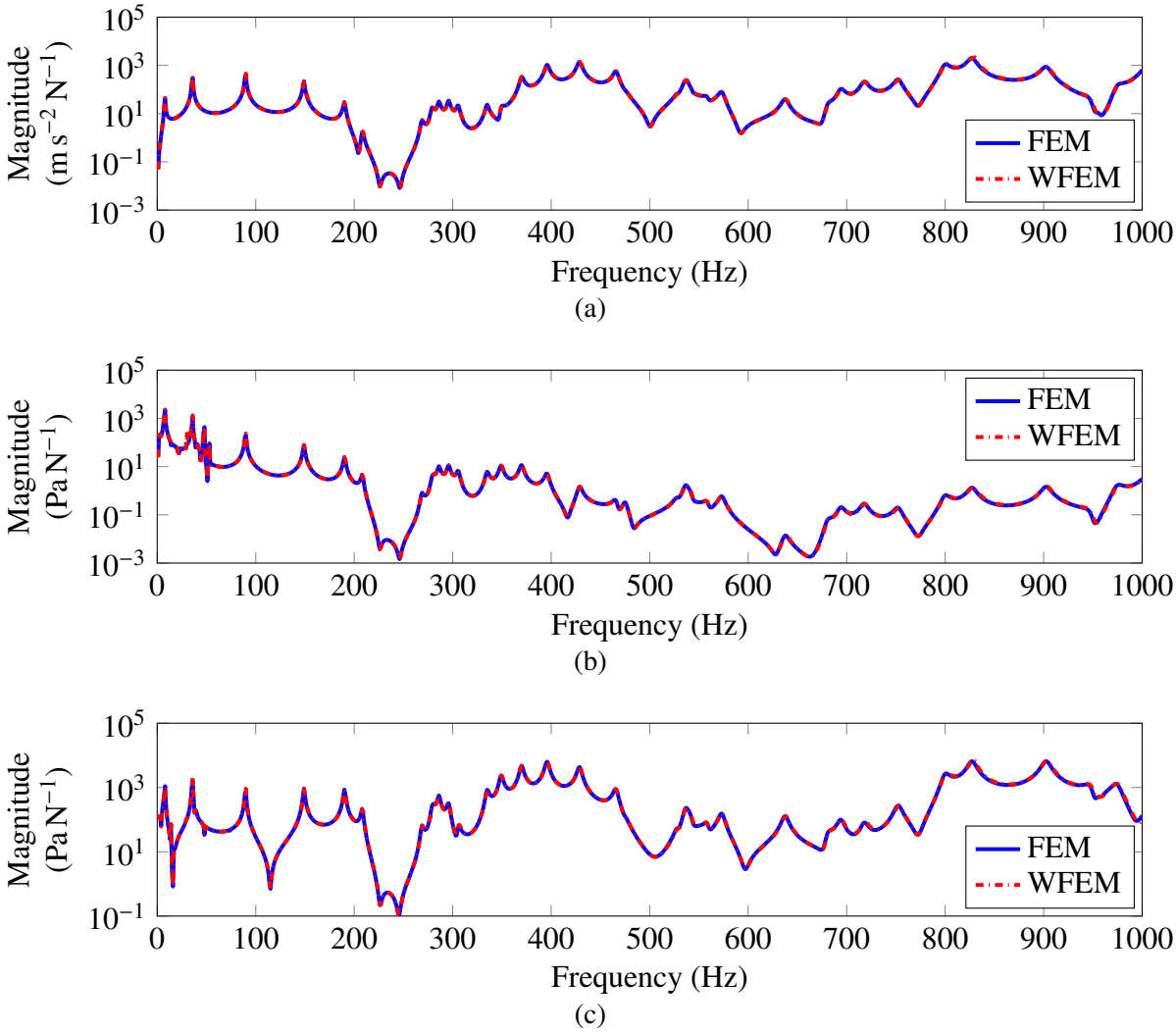


Figure 5: Frequency response functions computed by the FEM and WFEM for the input and output locations shown in Fig. 4: a) output acceleration; b) output pressure #1 (at the fluid free-surface); and c) output pressure #2 (at an interior node of the fluid). For the WFEM, a unit cell reduced-order model was employed, with the uncoupled structural and acoustic-fluid internal DoFs ($\mathrm{U_I}$ and $\mathrm{P_I}$ DoF sets) reduced through the CB method ($n_{\mathrm{CB}} = 5$), interior coupled DoFs located at the fluid–structure interface (Γ_{I} DoF set) reduced through L-CC ($n_{\text{L-CC}_{\mathrm{I}}} = 5$), and boundary DoFs ($\mathrm{U_L}$, $\mathrm{P_L}$, Γ_{L}, $\mathrm{U_R}$, $\mathrm{P_R}$, and Γ_{R} DoF sets) likewise reduced through L-CC ($n_{\text{L-CC}_{\mathrm{B}}} = 2$ and $\tau_{\mathrm{MAC}} = 0.90$). Eigenvectors were classified as SMs/N-SMs using $\tau_{\mathrm{SMs}} = 0.99$.

Figure 5 illustrates that the FRFs computed using the WFEM and the reduced-order unit cell model agree very well with the FEM-reference solutions. In fact, the results reveal that accurate responses are obtained regardless of whether they are evaluated in the structural (Fig. 5a) or acoustic-fluid domain, with the latter considered either at the fluid free-surface (Fig. 5b) or within the fluid interior (Fig. 5c). The WFEM can therefore very satisfactorily replace the traditional FEM.

Quantitatively, the accuracy of the reduced-order model can be assessed by calculating i) the RE between the resonance frequencies identified from the FRFs computed using the FEM and WFEM, which is associated with inaccuracies in the inertia and stiffness properties of the system, and ii) the CSF between FRFs computed using the FEM and WFEM, quantifying discrepancies

in terms of amplitude [7]. Accordingly, Fig. 6 presents the REs and CSFs for the FRFs shown previously in Fig. 5. As can be observed, both error metrics remain very good regardless of whether they are evaluated for FRFs associated with the structural or fluid responses, at the fluid free-surface or within the fluid interior, confirming the very good (visual) agreement between the FEM and WFEM results observed in Fig. 5. That is to say, the REs remain very close to 0, never exceeding 0.5%, while the CSFs remain approximately equal to 1 throughout the whole frequency range. It should be clarified that, in Fig. 6b, the relatively low CSF of approximately 0.5, occurring at 30 Hz, is related to a meaningless peak in the corresponding WFEM-related FRF, shown in Fig. 5b, ensuing as a consequence of instabilities (numerical issues) within the WFEM. This issue could be eliminated by decreasing the threshold value adopted for the MAC to $\tau_{\text{MAC}} = 0.80$, for example. However, since this peak is virtually unnoticeable in Fig. 5b and affects the system response only locally rather than as a whole, this action has not been pursued.

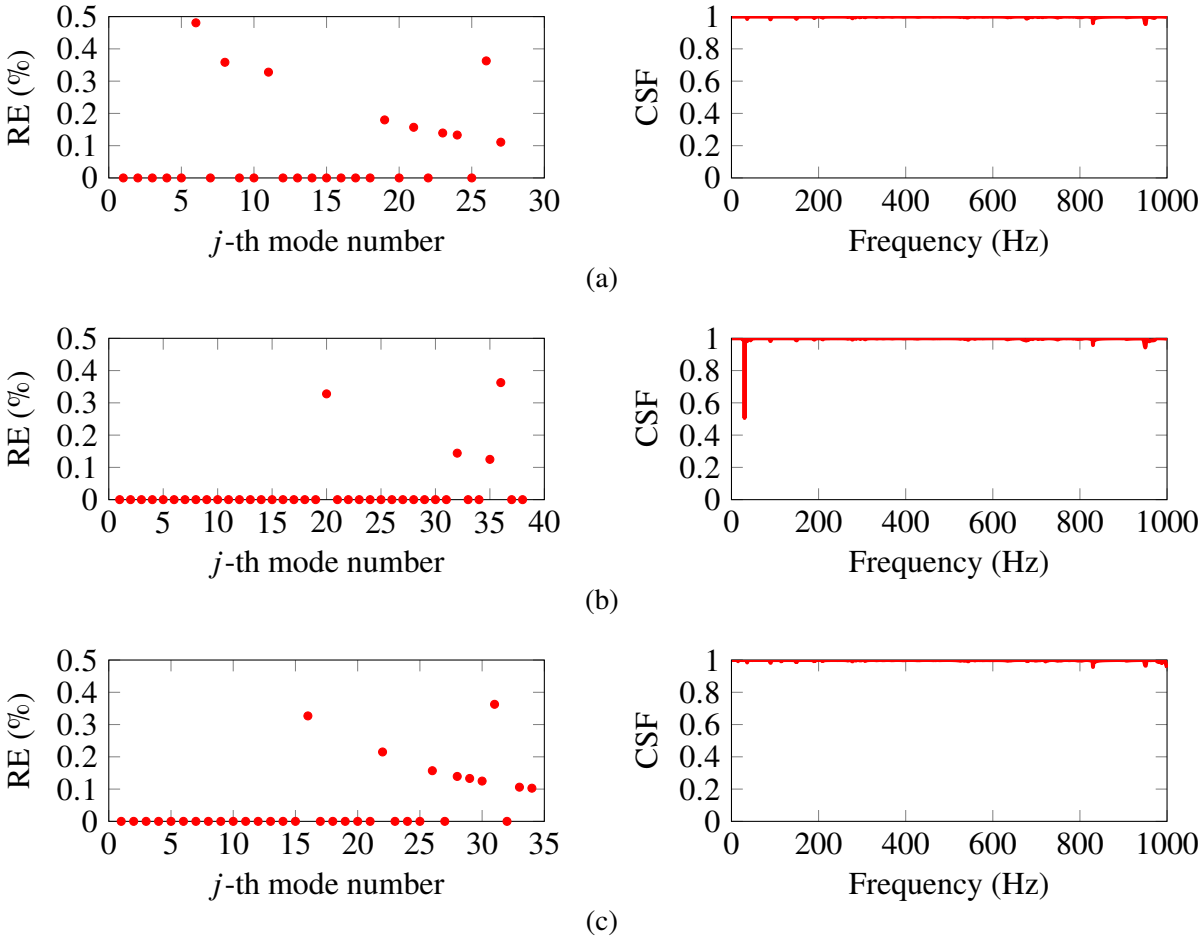


Figure 6: Relative errors and cross-signature scale factors computed for the frequency response functions previously shown in Fig. 5.

Lastly, Table 2 summarizes the timing data required to compute the FRFs previously shown in Fig. 5 using the WFEM and the FEM. The results show that the reduction of coupled structural and fluid internal DoFs (Γ_{I} DoF set) is the most computationally expensive task, requiring 5891 s to be completed. This relatively high computational cost is related to the computation of large numbers of eigenvectors when deriving $\boldsymbol{\Psi}_{\Gamma_{\text{I}}}$, Eq. (12), as a consequence of the low-frequency SMs arising not only from local modes, but also from global modes. It should be noted that,

to distinguish the eigenvectors into SMs and N-SMs, additional computational burden is introduced during the reduction of coupled structural and fluid internal DoFs, since the calculation of pressures ratios is required, as discussed previously. This arises because the proper mapping of pressure gradients within the acoustic-fluid necessitates eigenvectors represented in physical coordinates, rather than in mixed coordinates comprising modal and physical DoFs, as is the case when the local and global mode sets are computed. Recall that the reduction of the Γ_I DoF set is performed after the reduction of uncoupled structural and fluid internal DoFs.

The calculation of frequency-dependent wavemode amplitudes ($\mathbf{Q}$ and $\mathbf{Q}^*$) ranks second in Table 2, requiring 4672 s as a consequence of the relatively large linear system of equations solved in this step. Subsequently, the computation of wave modes ($\boldsymbol{\mu}$, $\boldsymbol{\mu}^*$, $\boldsymbol{\Phi}$, and $\boldsymbol{\Phi}^*$) takes 2720 s. Similarly to the calculation of wavemode amplitudes, matrices of relatively large size are involved in this step due to the moderate number of (modal) DoFs encountered at the unit cell interfaces (2×189), which directly influence the previous task. The time required to perform the reduction of uncoupled structural and fluid internal DoFs drops to 986 s, mainly because the computation of structural fixed-interface modes collected in $\boldsymbol{\Xi}_{U_I}$ does not involve determining any SM, although the associated matrices are large (cf. Table 1), and the size of matrices associated with the reduction of the acoustic-fluid domain is not excessive in this step. The reduction of boundary DoFs takes 605 s, as this step comprises matrices of much smaller size and, additionally, does not require global modes to be computed again (cf. Subsection 2.4). Other tasks which do not fall into the aforementioned categories, such as the import of FE data, matrix conditioning, identification of relevant equations, etc., require merely 47 s in Table 2.

Overall, the results in Table 2 show that the WFEM demands 16848 s to obtain the FRFs shown in Fig. 5, while this number increases to 480126 s within the FEM (which uses the direct method, as modal superposition is not available to solve the problem tackled in our work). Therefore, the WFEM together with the reduced-order unit cell model is able to speed up the dynamic analysis of the HPS considered herein by almost 30 times.

Task	Related equations	WFEM	FEM
Reduction of uncoupled structural and fluid internal DoFs (U_I and P_I DoF sets)	(5)–(8)	986	–
Reduction of coupled structural and fluid internal DoFs (Γ_I DoF set)	(9)–(13)	5891	–
Reduction of boundary DoFs (U_L, P_L, Γ_L, U_R, P_R, and Γ_R DoF sets)	(14)–(22)	605	–
Computation of wave modes ($\boldsymbol{\mu}$, $\boldsymbol{\mu}^*$, $\boldsymbol{\Phi}$, and $\boldsymbol{\Phi}^*$)	(25)–(27)	2720	–
Calculation of wavemode amplitudes ($\mathbf{Q}$ and $\mathbf{Q}^*$)	–	4672	–
Evaluation of the system's physical responses	(28), (29), (23)	1927	480126
Other (import of FE data, matrix conditioning, identification of relevant equations, etc.)	(1)–(4)	47	–
Total	–	16848	480126

Table 2: Wall-clock times, in seconds, for the calculation of the FRFs depicted in Fig. 5.

4 CONCLUSIONS

This work introduced a novel model reduction strategy for unit cells of HPSs exhibiting strong fluid–structure interactions and linear sloshing. Within the proposed MOR scheme, uncoupled

structural and fluid internal DoFs of a unit cell are initially reduced using the CB method, while preserving those DoFs related to fluid–structure interfaces and the left and right boundaries of the unit cell. Then, the internal DoFs related to the fluid–structure interface are reduced using the L-CC MOR method, employing three sets of Ritz vectors that account for local modes, rigid-body modes, and low-frequency flexible-body modes, proper to take into consideration strong fluid–structure interaction. Finally, the unit cell boundary DoFs are likewise reduced using the L-CC MOR approach, taking into account three distinct bases during the MOR process and respecting conditions necessary to satisfy the Bloch–Floquet theorem applied afterward within the WFEM. A reduced-order model was derived for the unit cell of a HPS exhibiting a compliant geometry, thin walls, and "soft" material, and hosting a heavy fluid, allowing a reduction of more than 85% of the number of equations of the unit cell. Frequency response functions computed using the WFEM showed very good agreement with reference results obtained with the FEM. The error analysis indicated that resonance frequencies can be accurately identified from FRFs obtained with the WFEM relative to the FEM, while also providing very good amplitude matches, as demonstrated by low REs, and CSFs close to one. The results of the study also demonstrate that the WFEM together with the reducer-order unit cell model is able to significantly speed up the analysis of a HPS, being almost 30 times faster than the traditional FEM. This work therefore opens new avenues for the efficient dynamic analysis of periodic structures by combining reduced-order unit cell models with the WFEM.

5 ACKNOWLEDGMENTS

This study was financed, in part, by the São Paulo Research Foundation (FAPESP), Brasil. Process Numbers #2018/15894-0, #2023/11207-7 and #2024/07549-2. All authors are grateful to FAPESP for the provided grants. V. M. S. Santos also acknowledges the Brazilian Coordination for the Improvement of Higher Education Personnel (CAPES). M. Ouisse acknowledges the graduate school EIPHI (project ANR-17-EURE-0002).

REFERENCES

[1] K. Billon et al. "Mechanics and band gaps in hierarchical auxetic rectangular perforated composite metamaterials". In: *Compos. Struct.* 160 (2017). DOI: 10.1016/j.compstruct.2016.10.121.

[2] K. Tang et al. "Dynamic cloaking of a diamond-shaped hole in elastic plate". In: *Appl. Phys. Lett.* 122 (2023). DOI: 10.1063/5.0123575.

[3] X.-F. Li et al. "Tunable Unidirectional Sound Propagation through a Sonic-Crystal-Based Acoustic Diode". In: *Phys. Rev. Lett.* 106 (2011). DOI: 10.1103/physrevlett.106.084301.

[4] V. Laude. "Principles and properties of phononic crystal waveguides". In: *APL Mater.* 9 (2021). DOI: 10.1063/5.0059035.

[5] T. Hoang, D. Duhamel, and G. Foret. "Wave finite element method for waveguides and periodic structures subjected to arbitrary loads". In: *Finite Elem. Anal. Des.* 179 (2020). DOI: 10.1016/j.finel.2020.103437.

[6] D. S. Claro, V. Denis, and J.-M. Mencik. "A wave finite element approach for the vibroacoustic analysis of fluid-filled pipes with joints and defects". In: *Wave Motion* 138 (2025). DOI: 10.1016/j.wavemoti.2025.103576.

[7] V. M. S. Santos, T. P. Sales, and M. Ouisse. "Improving the computation of forced responses of periodic structures by the wave-based finite element method via a modified generalized Bloch mode synthesis". In: *Finite Elem. Anal. Des.* 245 (2025). DOI: 10.1016/j.finel.2025.104314.

[8] R. R. Craig Jr. and A. J. Kurdila. *Fundamentals of structural dynamics*. Second edition. John Wiley & Sons, 2006. ISBN: 9780471430445.

[9] M. Géradin and D. J. Rixen. *Mechanical Vibrations. Theory and Application to Structural Dynamics*. Third edition. John Wiley & Sons, 2015. ISBN: 9781118900208.

[10] K. Lu et al. "A Review of Model Order Reduction Methods for Large-Scale Structure Systems". In: *Shock Vib.* 2021 (2021). DOI: 10.1155/2021/6631180.

[11] D. Krattiger and M. I. Hussein. "Generalized Bloch mode synthesis for accelerated calculation of elastic band structures". In: *J. Comput. Phys.* 357 (2018). DOI: 10.1016/j.jcp.2017.12.016.

[12] S. Boily and F. Charron. "The vibroacoustic response of a cylindrical shell structure with viscoelastic and poroelastic materials". In: *Appl. Acoust.* 58 (1999). DOI: 10.1016/s0003-682x(98)00070-x.

[13] Q. H. Tran, M. Ouisse, and N. Bouhaddi. "A robust component mode synthesis method for stochastic damped vibroacoustics". In: *Mech. Syst. Signal Pr.* 24 (2010). DOI: 10.1016/j.ymssp.2009.06.016.

[14] S. M. Kim et al. "A strongly coupled model reduction of vibro-acoustic interaction". In: *Comput. Method. Appl. M.* 347 (2019). DOI: 10.1016/j.cma.2018.12.029.

[15] V. M. S. Santos, T. P. Sales, and M. Ouisse. "A novel Generalized Bloch Mode Synthesis combined with the Wave-based Finite Element Method for modeling acousto-elastic periodic structures with strong fluid–structure interaction". In: *Comput. Struct.* (2026).

[16] M. Maess and L. Gaul. "Substructuring and model reduction of pipe components interacting with acoustic fluids". In: *Mech. Syst. Signal Pr.* 20 (2006). DOI: 10.1016/j.ymssp.2005.02.008.

[17] J. Herrmann, M. Maess, and L. Gaul. "Substructuring including interface reduction for the efficient vibro-acoustic simulation of fluid-filled piping systems". In: *Mech. Syst. Signal Pr.* 24 (2010). DOI: 10.1016/j.ymssp.2009.05.003.

[18] G. C. Everstine. "A symmetric potential formulation for fluid-structure interaction". In: *J. Sound Vib.* 79 (1981). DOI: 10.1016/0022-460x(81)90335-7.

[19] J.-M. Mencik and D. Duhamel. "A wave-based model reduction technique for the description of the dynamic behavior of periodic structures involving arbitrary-shaped substructures and large-sized finite element models". In: *Finite Elem. Anal. Des.* 101 (2015). DOI: 10.1016/j.finel.2015.03.003.

[20] V. M. S. Santos. "Numerical Investigation of Wave Propagation in Beams Coupled to Metastructures Combining Spectral and Wave-Finite Element Methods". MA thesis. Aeronautics Institute of Technology, 2022.

[21] V. M. S. Santos, T. P. Sales, and M. Ouisse. "Investigation of a Novel Metastructure with Trapped, Fluid-Filled Unit Cells". In: *Advances in Structural Vibration*. Ed. by P. Kurka and M. Pereira. Springer, 2025. DOI: 10.1007/978-3-031-71540-2_9.